3

Numerical methods

3.1 Introduction

A finite volume multigrid method has been used to solve the system of partial differential equations describing thermohaline convection in porous media (equations (2.16) and (2.17), together with either (2.18) or (2.19). This method was originally developed for convection of purely viscous fluids at infinite Prandtl number [*Trompert and Hansen*, 1996]. General characteristics of this method are first, a subdivision of the model domain into control volume cells. Next, the equations are discretized in space and time separately, in a conservative way (sections 3.2 and 3.3). The accuracy of the discretization is of second order. Finally, the resulting system of algebraic equations is solved line-by-line with a multigrid method in which a basic iterative method is used: Gauss-Seidel or damped Jacobi[1].

The advantage of using one of these simple iterative methods is that the amount of computation time needed for each iteration step is small, as compared to more advanced iterative methods [*Golub and Van Loan*, 1993]. However, the rate of convergence deteriorates as the size of the problem grows. The reason for that is that the high-frequency Fourier modes of the error are damped much more rapidly than the low-frequency ones. Here, the error is defined as the difference between the iterated approximated solution and the exact solution of the discrete system of equations. High-frequency Fourier modes are modes that cannot be represented on coarser grids. The damping of the low-frequency modes becomes even worse for an increasing problem size.

In the multigrid method, the low-frequency part of the error is approximated on coarser grids. Subsequently, this approximation is used to improve the fine grid solution. A detailed description of the multigrid method used in this thesis, is given by *Trompert and Hansen* [1996]. For an extensive discussion of multigrid methods, the reader is referred to *Hackbush* [1985] and *Wesseling* [1992]. With the multigrid method, computation time needed for one iteration scales linearly with the number of cells. Consequently, problems with high spatial resolution can be solved very economically, as compared with direct solution methods. In the final section, the results of a number of benchmark tests of flow in porous media are discussed.

[1] Optimization of the method to the computer platform used discriminates between these two methods: Gauss-Seidel is used on scalar machines, damped Jacobi on vector platforms.

3.2 The spatial discretization

A Cartesian geometry is divided in rectangular shaped cells $\Omega_{i,k}$. A control-volume discretization is used to discretize the non-dimensional equations (2.16)-(2.17), together with (2.18) or (2.19). All three unknowns (pressure, temperature and compositional concentration) are defined at the center of each cell (see Figure 3.1). The velocity normal to a cell face is defined at the center of that cell face. Note that the velocity vector is not unknown, but can be calculated directly from the pressure and density distribution by Darcy's law. The equations can all be written in the general form

$$\frac{\partial Q}{\partial t} + \frac{\partial F}{\partial x} + \frac{\partial G}{\partial z} = f, \tag{3.1}$$

By using midpoint quadrature, all equations are integrated over the control volume $\Omega_{i,k}$ with center (x_i, z_k) and sides Δx and Δz.

$$\left(\frac{\partial Q}{\partial t}\right)_{i,k} \Delta z \Delta x + \Delta z\,(F_{i,k} - F_{i-1,k}) + \Delta x\,(G_{i,k} - G_{i,k-1}) = f_{i,k}\Delta z \Delta x. \tag{3.2}$$

In thermochemical convection at Rayleigh numbers relevant to porous or partially molten environments, thin horizontal boundary layers develop. Moreover, physical parameters like permeability may vary significantly with depth. Therefore, we allow for a non-uniform grid in the z-direction. The grid is uniform in the x-direction.

All derivatives are discretized in a straight-forward manner. The diffusion coefficients are computed at the cell centers. However, the discretization of equation (3.2) requires the diffusion coefficients at the midpoint of cell faces. Such a diffusion coefficient at a cell edge is computed by using a harmonic interpolation based on continuity of fluxes [*Patankar*, 1981]. For example, on a uniform grid in one dimension the harmonic average of a diffusion coefficient φ is:

$$\varphi_c = \frac{2\varphi_i \varphi_{i+1}}{\varphi_i + \varphi_{i+1}}. \tag{3.3}$$

This leads to a more accurate discretization, when the diffusion coefficient φ is discontinuous. This is often the case in the momentum, energy and species equations.

3.2.1 Diffusive and dispersive fluxes

For the spatial discretization of the diffusive fluxes in equation (3.2), a central approximation is used. For example, on a nonuniform grid in one dimension, the diffusive thermal flux $\partial T/\partial x$ on cell boundary $i+\frac{1}{2}$ separating cell Ω_i from Ω_{i+1}, is computed in the following manner:

$$\left(\frac{\partial T}{\partial x}\right)_{i+1/2} = \frac{T_{i+1} - T_i}{x_{i+1} - x_i} \tag{3.4}$$

where T_i is the temperature at the center of cell Ω_i and x_i the center of cell Ω_i.

The diagonal terms of the dispersive fluxes in the tensorial species equation are calculated in a similar way as the thermal diffusion terms in equation (3.4). For the off-diagonal terms, on the other hand, a vertical derivative has to be calculated on a vertical cell face and a

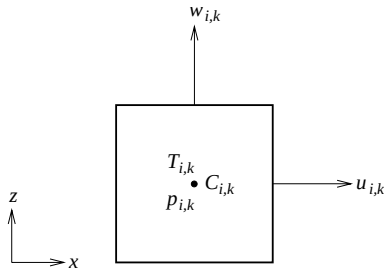

Figure 3.1: The grid cell $\Omega_{i,k}$ used in the cell-centered discretization together with the variables associated with this cell.

horizontal one on a horizontal cell face. For example, the vertical derivative of chemical concentration on a vertical cell face is discretized as

$$\left(\frac{\partial C}{\partial z}\right)_{i+1/2} = \frac{C_{i+1,k+1} + C_{i,k+1} - C_{i+1,k-1} - C_{i,k-1}}{2\left(z_{k+1} - z_{k-1}\right)} \tag{3.5}$$

3.2.2 Advective fluxes

The upwind-biased Fromm scheme is used for the approximation of the advective thermal fluxes. This scheme interpolates the temperature at cell faces using two upwind points and one downwind point. It uses a Taylor series expansion for the interpolation using temperature at cell centers and an approximation to the first derivative. In one dimension, the advective thermal flux becomes:

$$\begin{aligned}(qT)_{i+1/2} \quad = \quad & \max(q_i, 0)\left(T_i + \left(x_{i+1/2} - x_i\right)\frac{T_{i+1} - T_{i-1}}{x_{i+1} - x_{i-1}}\right) \\ & + \min(q_i, 0)\left(T_{i+1} + \left(x_{i+1/2} - x_i\right)\frac{T_{i+2} - T_i}{x_{i+2} - x_i}\right),\end{aligned} \tag{3.6}$$

where q_i is the normal velocity at cell boundary $i+1/2$ and $x_{i+1/2}$ the spatial coordinate of the cell boundary $i+\frac{1}{2}$. Method (3.6) can produce some over- and undershoot near sharp interfaces, which may develop in the advection-dominated chemical field. Although the wiggles produced by the upwind-biased scheme are small, they may lead to non-physical negative concentrations C. One way to avoid these instabilities is by changing to a first order upwind-biased scheme. However, such a scheme leads to more numerical diffusion as compared to second order upwind-biased methods and is, therefore, not very accurate. Another way to suppress the wiggles is by considering flux-limiter methods [*Sweby,* 1984]. These methods have been developed to preserve the monotonicity of the solution, while the accuracy remains higher than first-order upwind methods.

Here, we consider the flux-limited Fromm scheme, as derived by *Hundsdorfer and Trompert* [1994], for the advection of C. Essentially, this scheme is second order but shifts to a first-order approximation near sharp interfaces. Let us now derive the flux-limiter scheme in a one dimensional domain, for the case when $q > 0$. In the conservation form, the advective flux is then written as:

$$(qC)_{i+1/2} = q\left(C_i + \left(d_0 + d_1\theta_i\right)\left(C_{i+1} - C_i\right)\right), \quad \text{with} \tag{3.7}$$

$$\theta_i = \frac{C_i - C_{i-1}}{C_{i+1} - C_i} \text{ and } d_0 = d_1 = \frac{z_{i+1} - z_i}{z_{i+2} + z_{i+1} - z_i - z_{i-1}}. \tag{3.8}$$

Note that the Fromm scheme (3.6) is obtained from these equations, for an equidistant grid (for which $d_0 = d_1 = 1/4$). When we now rewrite $(qC)_{i+1/2}$ as

$$(qC)_{i+1/2} = q\left(C_i + \psi(\theta_i)\left(C_{i+1} - C_i\right)\right), \quad \text{with} \tag{3.9}$$

$$\psi(\theta_i) = \max\left(0, \min\left(1, d_0 + d_1\theta, \theta\right)\right), \tag{3.10}$$

it can be shown that the condition for positivity is satisfied when the Courant number $\nu = q\Delta t/\Delta x \leq 1/2$ [*Hundsdorfer and Trompert*, 1994]. The function ψ determines a correction on the upwind flux $(qC)_{i+1/2}$, and is called the flux limiter.

In this way, the conservation properties of the finite volume discretization are sustained. In other words, the mass balance of chemical concentration is preserved. Moreover, the maximum principle theorem applies, which says that the unknown parameter can only take its (local) maxima at the boundaries of the domain. Finally, the total variation of the solution does not increase (TVD-scheme). In case $q < 0$, equation (3.9) becomes

$$(qC)_{i+1/2} = q\left(C_{i+1} + \psi\left(\frac{1}{\theta_{i+1}}\right)\left(C_{i+1} - C_i\right)\right). \tag{3.11}$$

3.3 Time integration

3.3.1 Energy equation

Time integration of the energy equation (2.17) is carried out by a second order accurate explicit-implicit method. The implicit Crank-Nicolson method is used for the diffusion and an explicit Adams-Bashforth scheme for the advection. For variable time step sizes, this discretization is defined as

$$\begin{aligned} T^{n+1} &= T^n - \frac{1}{2}\Delta t\left[\left(2 + \frac{\Delta t}{\Delta t_p}\right)\nabla\cdot(\mathbf{q}T)^n - \frac{\Delta t}{\Delta t_p}\nabla\cdot(\mathbf{q}T)^{n-1}\right] \\ &\quad + \frac{1}{2}\Delta t\left[\nabla^2 T^{n+1} + \nabla^2 T^n\right], \end{aligned} \tag{3.12}$$

where $\Delta t = t^{n+1} - t^n$ is the current time step size and $\Delta t_p = t^n - t^{n-1}$ the previous one. The superscripts denote time levels. This method is only conditionally stable. In order to avoid instabilities, a time step criterion is chosen as

$$\Delta t = 0.5/\left(\frac{\|u\|_\infty}{\Delta x} + \|\frac{w}{\Delta z}\|_\infty\right), \tag{3.13}$$

where Δx and Δz are the cell sizes in each coordinate direction and $\|.\|_\infty$ is the maximum norm. Since the grid is nonuniform in z-direction, the maximum of $w/\Delta z$ is computed. The factor 0.5 is empirically determined so that, on the one hand, time step sizes are not extremely small and, on the other hand, instabilities are avoided.

3.3.2 Equation of species

The implemented temporal discretizations differ for the two species equations (2.18) and (2.19). For the scalar effective dispersion model, the time discretization is almost similar to the explicit-implicit method (3.12), as employed for the energy equation:

$$\begin{aligned} C^{n+1} &= C^n - \frac{1}{2\phi^*}\Delta t \left[\left(2 + \frac{\Delta t}{\Delta t_p}\right) \nabla \cdot (\mathbf{q}C)^n - \frac{\Delta t}{\Delta t_p} \nabla \cdot (\mathbf{q}C)^{n-1} \right] \\ &\quad + \frac{1}{2\phi^*}\Delta t \left[\nabla \cdot \left(\frac{1}{Le_{\text{eff}}} \nabla C \right)^{n+1} + \nabla \cdot \left(\frac{1}{Le_{\text{eff}}} \nabla C \right)^{n} \right]. \end{aligned} \tag{3.14}$$

Since the chemical components are advected with a velocity $\mathbf{q}/\phi^*$, rather than $\mathbf{q}$, the time step size Δt_{C1} is computed as follows:

$$\Delta t_{C1} = 0.5 / \left(\frac{\|u/\phi^*\|_\infty}{\Delta x} + \| \frac{w/\phi^*}{\Delta z} \|_\infty \right). \tag{3.15}$$

In case a tensorial dispersion model is employed (equation (2.19)), this explicit-implicit method may result in an ill-posed problem, when velocity and therefore mechanical dispersion becomes zero locally. In order to avoid instabilities, an explicit second order Adams-Bashforth scheme is employed for both advection and dispersion terms:

$$\begin{aligned} C^{n+1} &= C^n - \frac{1}{2\phi^*}\Delta t \left[\left(2 + \frac{\Delta t}{\Delta t_p}\right) \nabla \cdot (\mathbf{q}C - \mathbf{D}\nabla C)^n \right] \\ &\quad + \frac{1}{2\phi^*}\Delta t_p \left[\nabla \cdot (\mathbf{q}C - \mathbf{D}\nabla C)^{n-1} \right] \end{aligned} \tag{3.16}$$

Here, the limitation of the time step depends on both advective and dispersive fluxes. For this method, the time step size Δt_{C2} is chosen as:

$$\Delta t_{C2} = 0.5 / \left[\frac{\|u/\phi^*\|_\infty}{\Delta x} + \| \frac{w/\phi^*}{\Delta z} \|_\infty + 4 \left(\frac{\|D_{11}\|_\infty}{\Delta x^2} + \| \frac{D_{22}}{\Delta z^2} \|_\infty \right) \right]. \tag{3.17}$$

3.3.3 Practical stability criterion

For the time step criteria derived above, the velocity at the previous time step is used (see equations (3.13), (3.15) and (3.17)). These criteria are a good guess for the stability of the system of non-linear equations, but are not exact. Instabilities may arise when the solution field changes significantly over one time step. In order to avoid such instabilities, an additional practical stability criterion is considered. This criterion bounds the change in velocity between two successive time steps n and $n+1$. A time step size Δt_q is selected in the following manner (with ε small ($O(10^{-20})$)):

$$\Delta t_q = \frac{\text{TOL}\ \Delta t_p}{\Delta Q}, \quad \text{with} \quad \Delta Q = \| \frac{q_{rms}^{n+1} - q_{rms}^n}{q_{rms}^{n+1} + \varepsilon} \|_\infty, \tag{3.18}$$

where TOL is a user-defined tolerance, here chosen to be 0.1. The time step chosen is the minimum of time steps determined by the stability of the integration methods (see equations (3.13), (3.15), and (3.17)) and the limitation of the change in velocity (equation (3.18)):

$$\Delta t = \min \left(\Delta t_T, \Delta t_{C1} \text{ or } \Delta t_{C2}, \Delta t_q \right). \tag{3.19}$$

3.4 Benchmark results

In this section, the results of benchmark tests of pure thermal, thermochemical and chemical convection in a porous medium are discussed.

3.4.1 Thermal convection benchmarks

Validation of the code is first accomplished by comparison with published results on pure thermal driven convection in a closed, square domain. The dimensionless temperature is fixed to 1 at the bottom and 0 at the top, while no heat is allowed to enter or leave the domain through the vertical sides. We obtained both solutions for Rayleigh numbers in the range $Ra_T = 0 - 800$. The solutions presented hereinafter were obtained using a mesh of 64 x 64 control cells, except for the solutions equal to $Ra_T = 500$ and above which were computed with 128 x 128 cells. The grids are refined at the top and bottom of the domain, in order to resolve the thermal boundary layers.

The numerical model used here predicts correctly the onset of convection at $Ra_T = 39.5$, as estimated from linear stability analysis [e.g. *Nield and Bejan*, 1992]. From this first point of bifurcation up to $Ra_T = 390$, single-cellular flow is steady, while the intensity of the convective motion increases with the Rayleigh number (see Table 3.1). The heat transport results of the employed model match closely those of laboratory or other numerical experiments [*Caltagirone*, 1975; *Steen and Aidun*, 1988; *Cherkaoui and Wilcock*, 1999]. Here, the dimensionless heat transport through the top, the Nusselt number Nu_T, is defined as:

$$Nu_T = -\overline{\frac{\partial \hat{T}}{\partial \hat{z}}} \; ; \; \hat{z} = 0, \tag{3.20}$$

where the overbar implies a horizontal average. Above $Ra_T = 390.7$, the thermal boundary layers of a single convection cell with aspect ratio 1 are unstable [*Steen and Aidun*, 1988]. For $Ra_T = 500$, 540 and 800 the flow is simulated for periods long enough to determine accurately the frequencies involved with the unstable boundary layers. Figure 3.2 shows the temperature field of the simulation at $Ra_T = 540$. Tongue-like disturbances of the boundary layers grow in amplitude while they are advected towards the vertical sides of the domain [*Kimura et al.*, 1986]. These blobs are also visible in the vertical plumes along the vertical boundaries.

Due to these thermal disturbances, the Nusselt number oscillates periodically with two basic frequencies (figure 3.2b,c). The frequencies of the spectral peaks are in good agreement with those observed in the experiments of *Caltagirone and Fabrie* [1989] and *Cherkaoui and Wilcock* [1999] (see Table 3.2). The model also resolves the reverse transition from the multiple frequency to the single frequency regime at larger higher Rayleigh number, as predicted

Ra_T	Nu_T			
	This study	*Caltagirone* [1975]	*Steen and Aidun* [1988]	*Cherkaoui and Wilcock* [1999]
50	1.450	1.44	1.450	1.450
100	2.643	2.65	2.651	2.647
200	3.806	3.81	3.810	3.801
300	4.511	4.52	4.523	4.519

Table 3.1: (a) Comparison of the Nusselt number for steady, unicellular thermal convection.

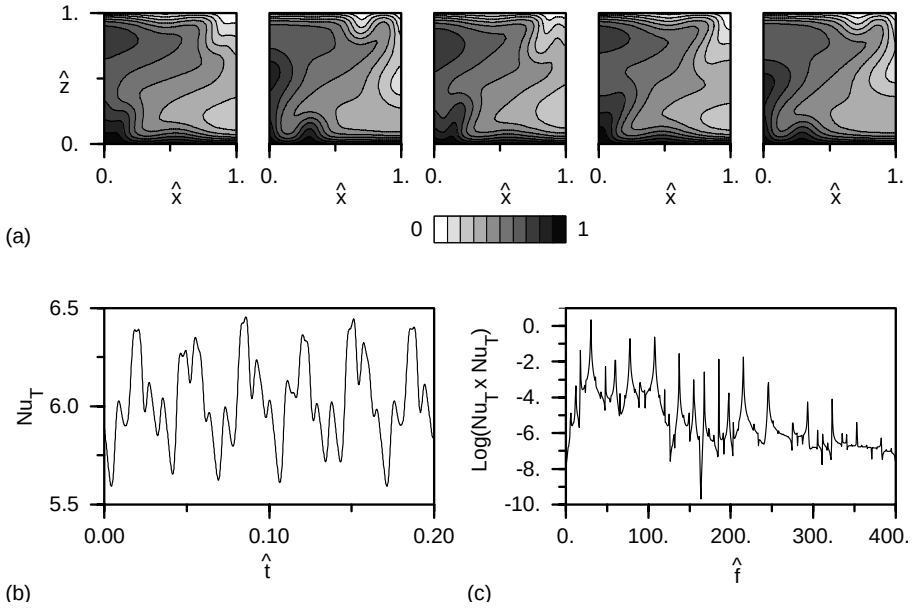

Figure 3.2: Unsteady convection in a square domain at $Ra_T = 540$. (a) Evolution of the temperature over one oscillatory cycle. Dark (light) shading denotes a high (low) temperature (see legend). (b) Nusselt number as a function of time. (c) Power spectrum of the Nusselt number, of which the mean is subtracted.

by *Kimura et al.* [1986]. For instance, at $Ra_T = 800$, the Nusselt number is characterized by one prevailing frequency. The frequency of $f = 287.2$ is in good agreement with published results, like is its amplitude in the power spectrum (compare with *Cherkaoui and Wilcock*, [1999], their Figure 1).

3.4.2 Thermochemical convection benchmark

Next, the results of a thermochemical convection simulation are compared with those obtained by *Rosenberg and Spera* [1992]. The scalar dispersion model is used. An initially cold and compositionally depleted fluid in a square domain with impermeable sides is heated and salted from below. The dimensionless temperature and chemical concentration are equal to 1 at the bottom, while at the top both quantities are fixed to 0. The vertical walls are insu-

	This study			*Caltagirone and Fabrie* [1989]			*Cherkaoui and Wilcock* [1999]		
Ra_T	$\overline{Nu_T}$	$\hat{f}_1$	$\hat{f}_2$	$\overline{Nu_T}$	$\hat{f}_1$	$\hat{f}_2$	$\overline{Nu_T}$	$\hat{f}_1$	$\hat{f}_2$
500	5.86	102.3	27.6	5.86	101.5	28.2	5.82	100.2	28.0
540	6.04	107.6	29.7	5.07	111.0	30.8	6.03	108.1	29.6
800	9.07	287.2	–	9.42	296.0	–	9.14	299.7	–

Table 3.2: Comparison of the average Nusselt number and the characteristic frequencies $\hat{f}_1$ and $\hat{f}_2$ for unsteady thermal convection.

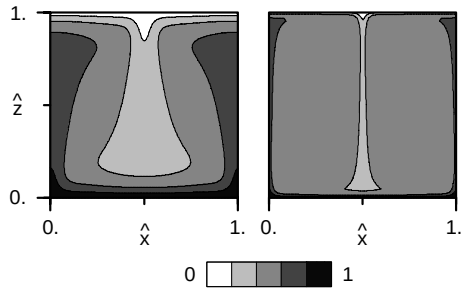

Figure 3.3: Steady-state solution of thermochemical convection in a square domain. Parameters are $Ra_T = 600$, $R_\rho = 0$ and $Le_{\text{eff}} = 20$. Dark (light) shading denotes a high (low) temperature or composition (see legend).

lators with respect to heat and solute transport. The simulations are obtained on various grids for the passive tracer case (the chemical field advects and diffuses but does not give rise to density differences), for the parameters $Ra_T = 600, R_\rho = 0$ and $Le_{\text{eff}} = 20$. In all calculations two side-by-side steady cells develop (see Figure 3.3). The flow consists of hot and compositionally enriched rising fluid, in the center of the domain, while colder and depleted fluid sinks along the adiabatic and impermeable horizontal sides.

In Table 3.3, the values of the kinetic energy per unit mass KE, and the thermal and chemical Nusselt numbers $Nu_{T,C}$ are given for the various discretizations. Here, kinetic energy per unit mass is defined as:

$$KE = \frac{1}{2}\langle \hat{q}_{\hat{x}}^2 + \hat{q}_{\hat{z}}^2 \rangle, \tag{3.21}$$

where the brackets denote the global average. The chemical Nusselt number Nu_C is defined in a similar way, but then for chemical concentration instead of temperature:

$$Nu_C = -\overline{\frac{\partial \hat{C}}{\partial \hat{z}}}\ ;\ \hat{z} = 0. \tag{3.22}$$

Note that Nu_C is more sensitive to spatial resolution in the boundary layers than KE or Nu_T. The kinetic energy, on the other hand, is dominated by the higher velocities in the interior of the domain and, therefore, it is less sensitive to the exact boundary layer thickness. The solution converges quadratically to the 'exact' solution when increasing the number of cells. This confirms the second order spatial accuracy.

This study					
Number of cells	*Grid*	*KE*	Nu_T	Nu_C	Nu_C/Nu_T
256	graded	1609	6.522	22.75	3.49
1024	graded	1669	6.610	28.09	4.25
4096	graded	1685	6.628	29.52	4.45
16384	graded	1689	6.632	29.65	4.47
Rosenberg and Spera [1992]					
2240	graded	1690	6.64	29.6	4.46

Table 3.3: Spatial resolution test and comparison for steady-state thermochemical convection ($Ra_T = 600, Ra_C = 0, Le_{\text{eff}} = 20$).

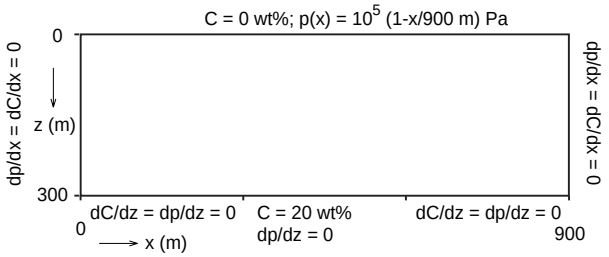

Figure 3.4: Geometry and boundary conditions of HYDROCOIN case 5 salt dome problem.

For a comparable number of nodes (*Rosenberg and Spera* [1992] used triangular elements with quadratic shape functions, which results in around 3 nodes per element), the values of KE and thermal and compositional Nusselt numbers agree within less than one percent with the values of Rosenberg and Spera. From elementary scaling it can be derived that $Nu_C/Nu_T = Le^{1/2}$, which in this case is $Le^{1/2} \approx 4.47$. Clearly, the ratio of the Nusselt numbers converges to this value for increasing number of cells.

3.4.3 Chemical convection benchmark

This test concerns the Hydrological Code Intercomparison (HYDROCOIN) project case 5: an idealized shallow groundwater flow system overlies a subcropping salt dome [*OECD*, 1988, 1992]. While a pressure gradient imposed at the top boundary drives the fluid along the surface of the salt dome, the dome itself represents the source of salt and brine in the active flow system. For simulation of this problem, the advanced dispersion model (2.19) is used.

The geometrical setup and boundary conditions are shown in Figure 3.4. The system is a two-dimensional cross-section of an 900 m wide and 300 m deep homogeneous, isotropic aquifer which is recharged by fresh water at the surface. The side and bottom boundaries are impermeable and insulators for solute flux, while the top boundary is represented by a linearly varying specified-pressure condition. These boundary conditions induce flow from left to right, but does not predetermine the rates of recharge and discharge nor the separation point between the in- and outflow zones. The concentration associated with the recharge is equal to zero. The fluid is assumed to be isothermal and isoviscous.

The salt dome is impermeable, so that salt is released into the active flow system only by diffusive or dispersive processes which are driven by a gradient in chemical concentration. The top of the salt dome, positioned at the central third of the bottom boundary, is exposed to circulating groundwater in the overlying aquifer, slowly releasing saturated brine by a diffusive/dispersive process. Note that the salt dome is represented by a constant-concentration at the the lower horizontal cell faces of the lowermost cells, which are positioned exactly at the bottom of the domain. The original problem was set up in a way that molecular diffusion of the salt equals zero. The properties assigned to the flow and transport are given in Table 3.4.

The solution to this problem is highly nonlinear and represents a balance among advection and hydrodynamic dispersion. The flow evolves towards a steady state solution, in which a brine pool has formed at the bottom (see Figure 3.5a). The positions of the isopleths agree closely with previously published results, obtained with other numerical models (e.g. *Konikow et al.* [1997], their Figure 4).

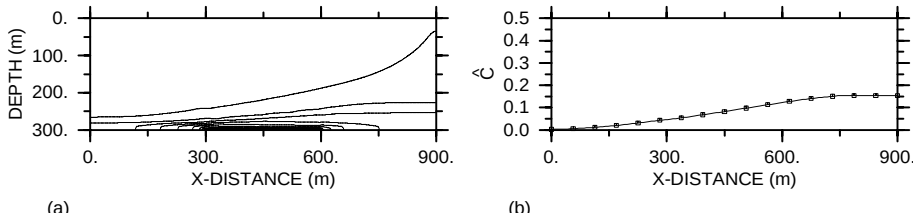

Figure 3.5: (a) Steady-state salt concentration (as mass fraction), for case 5 problem, using a non-equidistant 128 x 32 grid. (b) The brine concentration at a depth of 200 m.

Parameter	*Value*
Permeability (k)	10^{-12}m^2
Porosity (ϕ)	0.2
Dynamic viscosity (μ)	10^{-3}Pa s
Gravitational acceleration (g)	9.81 m s^{-2}
Reference freshwater density (ρ_f) at $\hat{C} = 0.0$	1000 kg m^{-3}
Reference brine density (ρ_s) at $\hat{C} = 1.0$	1200 kg m^{-3}
Longitudinal dispersivity (a_l)	20 m
Transversal dispersivity (a_t)	2 m
Effective molecular diffusivity (D_{mol})	0 m^2 s^{-1}
Initial fluid pressure at (x = 0 m, z = 0 m)	10^5 Pa

Table 3.4: Physical parameters of salt dome problem.

3.4.4 Conclusions

The above results show that the spatial and time discretization methods are second order accurate. The quantities derived here fall within a few percents of those obtained in the laboratory, from analytical methods and with numerical models. Considering the efficiency of the iterative multigrid method, the two-dimensional method is a powerful tool to study thermochemical convection problems in porous media at high resolution in time and space.